

Epitaxial Growth and Cracking Mechanisms of Thermally Sprayed Ceramic Splats

Lin Chen¹ · Guan-jun Yang¹

Submitted: 28 March 2017 / in revised form: 1 January 2018 / Published online: 24 January 2018
© ASM International 2018

Abstract In the present study, the epitaxial growth and cracking mechanisms of thermally sprayed ceramic splats were explored. We report, for the first time, the epitaxial growth of various splat/substrate combinations at low substrate temperatures (100 °C) and large lattice mismatch (− 11.26%). Our results suggest that thermal spray deposition was essentially a liquid-phase epitaxy, readily forming chemical bonding. The interface temperature was also estimated. The results convincingly demonstrated that atoms only need to diffuse and rearrange over a sufficiently short range during extremely rapid solidification. Concurrently, severe cracking occurred in the epitaxial splat/substrate systems, which indicated high tensile stress was produced during splat deposition. The origin of the tensile stress was attributed to the strong constraint of the locally heated substrate by its cold surroundings.

Keywords cracking · crystallographic orientation · epitaxial growth · lattice mismatch · substrate temperature

Introduction

Thermally sprayed ceramic coatings are widely used as thermal barrier coatings (TBCs) (Ref 1, 2), functional layers of solid oxide fuel cells (SOFCs) (Ref 3, 4), wear-resistant coatings (Ref 5), and abrasible seal coatings (Ref

6–8). Due to the special deposition processing, the coatings consist of splats (more precisely, crack patterns) piled up as layers. This indicates that they are essentially layered materials. Consequently, lamellar interfaces are important to the performance and service lifetime of thermally sprayed coatings. In addition, ubiquitous vertical cracks and lamellar gaps are two basic characteristics of thermally sprayed ceramic coatings (Ref 9–13). Therefore, a comprehensive understanding of the formation and evolution mechanisms of lamellar interfaces (including lamellar gaps) is of great importance for tailoring the performances of coatings.

Generally, interface bonding is categorized into chemical and mechanical bonding (Ref 14). Due to special deposition processing, the chemical bonding ratios of thermally sprayed ceramic coatings are considered to be no more than 32%, which results in their low strength, high porosity, and short lifetime (Ref 15, 16). Therefore, it seems difficult to form complete chemical bonding interfaces in thermally sprayed ceramic coatings. However, epitaxial growth of YSZ/LZ splats on single-crystal YSZ has been found when the substrate was preheated to merely higher than 100 °C before deposition (henceforth denoted as the substrate temperature) (Ref 17). This suggests that thermal spray deposition is essentially a liquid-phase epitaxy and therefore easily forms chemical bonding (Ref 17). Apparently, this was incompatible with the low chemical bonding ratio and high porosity. Therefore, the formation and evolution mechanisms of lamellar interfaces remain unclear, and further exploration is necessary.

Generally, lamellar gaps in thermally sprayed coatings were considered to be generated during splat deposition for some reasons such as low impact pressure (Ref 18, 19), condensates and adsorbates on substrate surfaces (Ref 20, 21). However, based on the model of impact pressure

✉ Guan-jun Yang
ygj@mail.xjtu.edu.cn

¹ State Key Laboratory for Mechanical Behavior of Materials, School of Materials Science and Engineering, Xi'an Jiaotong University, Xi'an 710049, Shaanxi, People's Republic of China

(Ref 18, 19), perfect bonding was formed in the central region, while not in the peripheral region due to low impact pressure (shown in Fig. 1 of Ref 18). Moreover, based on the model of condensates and adsorbates on the substrate surface, lamellar pores should be prohibited in the central region when the substrate is preheated to sufficiently high temperatures ($> 400\text{ }^{\circ}\text{C}$). This is because the condensates and adsorbates cannot be retained on the substrate surface at high substrate temperatures. Actually, the lamellar gaps almost existed in each segment in both the central and peripheral regions of splats at both low and high substrate temperatures (Ref 10–13). This was contrary to the conventional models mentioned above. Substantial transverse gaps were also found in homoepitaxial (YSZ on YSZ, and TiO_2 on TiO_2) and heteroepitaxial growth (LZ on YSZ) (Ref 17, 22, 23). Epitaxial growth indicated complete bonding (no gaps) between the splat and the substrate during solidification, which suggested that lamellar gaps in thermally sprayed coatings mainly resulted from transverse cracking.

The future of high-quality thermally sprayed ceramic coatings relies on effective control of lamellar interfaces. In this study, to explore the universal bonding mechanism at lamellar interfaces, epitaxial growth of various film/substrate combinations was systematically performed. The conditions for epitaxial growth of thermally sprayed ceramic splats were elaborated. Finally, the cracking of epitaxial films was discussed.

Experiment

Materials and Splat Deposition

To obtain more general results, five kinds of splats were identified, as shown in Table 1. In addition, to avoid any influences of the substrate surface profile and grain boundaries, all splats were deposited on (001) or (0001) planes of single-crystal substrate with well-polished surfaces ($R_a < 0.5\text{ nm}$). All substrates were square, with 10 mm width and 500 μm thickness. The edge orientations

Table 1 Powders and splat/substrate combinations

Splat	Powder shape	Powder size, μm	Substrate
TiO_2	Fused-crushed	30–50	$\text{TiO}_2/\text{Al}_2\text{O}_3/\text{YSZ}$
LCO	Agglomerate	15–45	YSZ
Cr_2O_3	Fused-crushed	38–50	$\text{YSZ}/\text{Al}_2\text{O}_3/\text{MgO}$
Al_2O_3	Fused-crushed	30–50	$\text{TiO}_2/\text{Al}_2\text{O}_3$
LSCO	Agglomerate	30–50	$\text{MgO}/\text{SrTiO}_3$

were $\langle 100 \rangle$ and $\langle 11\bar{2}0 \rangle$ for tetragonal/cubic and hexagonal substrates, respectively.

A commercial plasma spray system (GP-80, Jiujiang, China) and an external powder feeding injector were employed. Details of the experiments were similar to those in the former reports (Ref 17, 22, 23). To explore substrate temperature effects, the substrates were preheated to different temperatures (from 100 to 600 $^{\circ}\text{C}$) using a copper plate heater on which the substrates were placed. Additionally, to avoid extra calefaction of plasma arc to substrate, a shielding plate with several small holes was placed on the substrate.

Characterization of Coatings

Surface morphologies of the splats were examined using scanning electron microscopy (SEM, VEGA II-XMU, TESCAN, Czech Republic). Crystal orientations were characterized by the electron backscattered diffraction method (EBSD, AZTEC, OXFORD INSTRUMENTS, UK). Additionally, parts of cross-sectional morphologies were identified using a focused ion beam (FIB).

Results

To form coherent or semi-coherent interfaces, the capacity for epitaxial growth mainly relies on crystal structures and lattice mismatches between the films and substrates (Ref 24, 25). Generally, the allowable lattice mismatch is less than 10% for vapor phase epitaxial growth, 1% for liquid-phase epitaxial growth, and 0.1% for heterojunctions. In the present study, to obtain the universal bonding mechanism of thermally sprayed coatings, both homoepitaxial and heteroepitaxial growth with various splat/substrate combinations were identified at different substrate temperatures. Namely, the selected splats and substrates had tetragonal, cubic, and hexagonal structures. The lattice mismatch between splats and substrates at room temperature varied from -11.91 to $\sim 16\%$ to explore the limits of epitaxial growth by thermal spray deposition. Lattice mismatch herein is defined as the ratio of the difference of lattice constant between the film and the substrate to the lattice constant of the film. In addition, during SEM and EBSD observations, the substrate edge was always kept parallel to the edge of the SEM view field.

Bonding Condition for TiO_2 Splats

TiO_2 films/coatings are widely used as sterilizing material, electronic transportation layer in solar cells, etc. In the present study, the bonding conditions on tetragonal TiO_2 ,

hexagonal Al_2O_3 , and cubic YSZ were explored. Interestingly, epitaxial growth of TiO_2 splats on TiO_2 and Al_2O_3 substrates was found at substrate temperatures as low as 100°C , as shown in Fig. 1 and 2, respectively. Epitaxial TiO_2 splats presented regular morphologies. Based on topology (Ref 23), all crack patterns presented perfect hierarchical features. Interestingly, nanoscale dispersed particles emerged when the substrate temperature was higher than 500°C , as shown in Fig. 1(b) and 2(b), leading to rough surfaces. Apparently, the dispersed particles were incompatible with the underlying films and severely deteriorated the detection ability of EBSD. They probably resulted from evaporation or secondary precipitation during splat solidification.

In addition, rectangular crack patterns with $\langle 110 \rangle$ cracking (few along $\langle 100 \rangle$ directions) were produced on TiO_2 substrate, as shown in Fig. 1(a) and (b). They were consistent with the cleavage directions of TiO_2 (mainly $\langle 110 \rangle$ and few $\langle 100 \rangle$). Substrate spallation also occurred, forming tile-shaped patterns. Moreover, the EBSD orientation maps revealed epitaxial growth along the $\langle 100 \rangle$ direction, as shown in Fig. 1(c) and Table 2.

The lattice mismatch at room temperature between TiO_2 and Al_2O_3 was -3.57% . Interestingly, the splats on hexagonal Al_2O_3 substrate had triangle/parallelogram crack patterns, as shown in Fig. 2(a) and (b). Most of the cracks were along the $\langle 11\bar{2}0 \rangle$ or $\langle 01\bar{1}0 \rangle$ directions forming 60° angles with each other. Consistently, the $\langle 11\bar{2}0 \rangle$ direction was the closest-packed direction of hexagonal Al_2O_3 . The EBSD orientation maps revealed epitaxial growth along the $\langle 011 \rangle$ direction, as shown in Fig. 2(d) and Table 2. In addition, interface delamination readily occurred, as shown in Fig. 2(b). This was attributed to the much higher strength of Al_2O_3 than that of TiO_2 (Ref 26). The densities of vertical cracks were considerably high, which indicated that enormous tensile stress was produced during splat deposition (Ref 27–29).

The epitaxial growth of TiO_2 film on cubic YSZ substrate was difficult because the mismatch was as high as -11.91% at room temperature. Generally, intergranular cracking prevailed in polycrystalline TiO_2 leading to jagged crack morphologies. However, the morphology of localized cracks herein changed to quite straight when the substrate temperature was higher than 300°C , as shown in the insets of Fig. 3(a) and (b). As expected, the orientation maps revealed epitaxial growth along the $\langle 100 \rangle$ direction, as shown in Fig. 3(c) and Table 2. Due to the prohibitively high lattice mismatch, perfect epitaxial growth (similar to the case with TiO_2 or Al_2O_3 substrate) did not take place, even when the substrate temperature was as high as 600°C . In addition, weak trends of $\langle 110 \rangle$ and $\langle 100 \rangle$ cracking emerged, as shown in Fig. 3(a) and (b). The crack

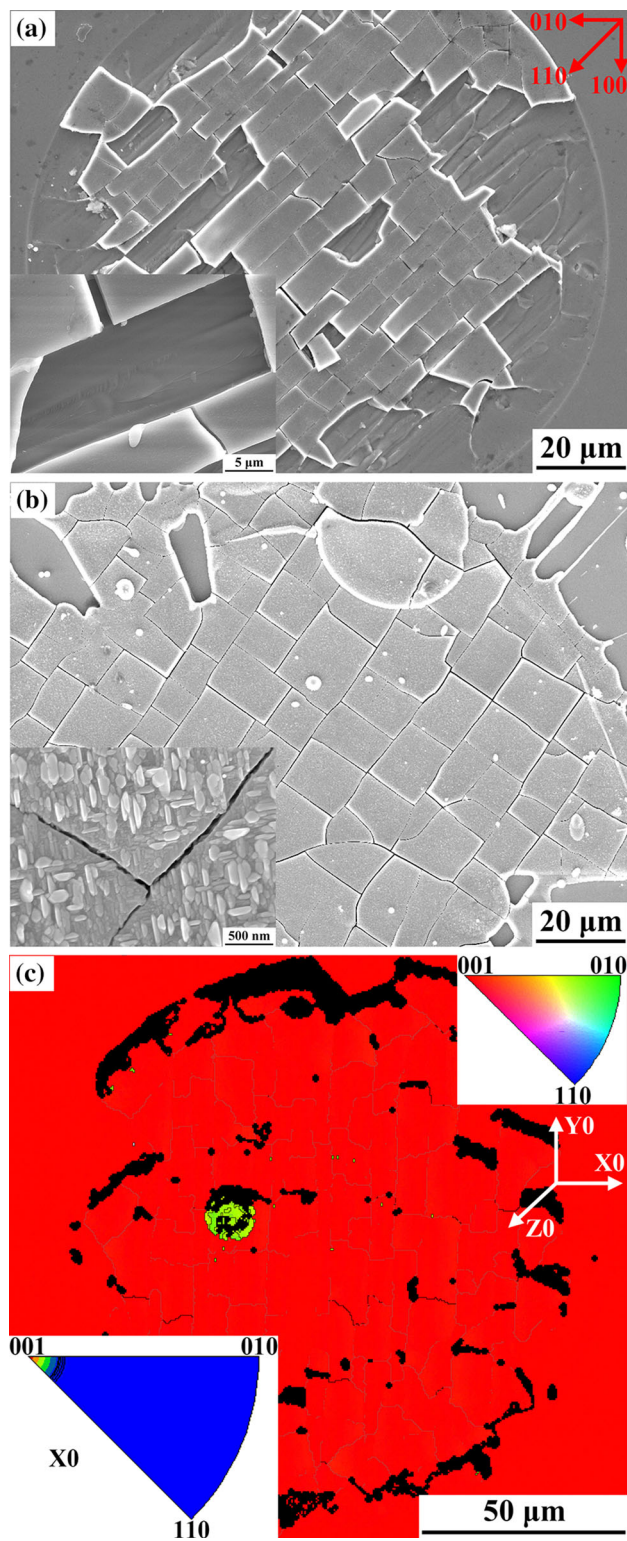


Fig. 1 Crack patterns of TiO_2 splat on TiO_2 substrate at the substrate temperature of (a) 100°C and (b) 600°C . The insets in (a) and (b) correspond to high magnification. (c): orientation maps of splat deposited at 200°C by EBSD which reveal epitaxial growth along the $\langle 100 \rangle$ direction. The insets in (c) correspond to inverse pole figures (IPFs, bottom left) and color key (top right) and the Euler coordinate system

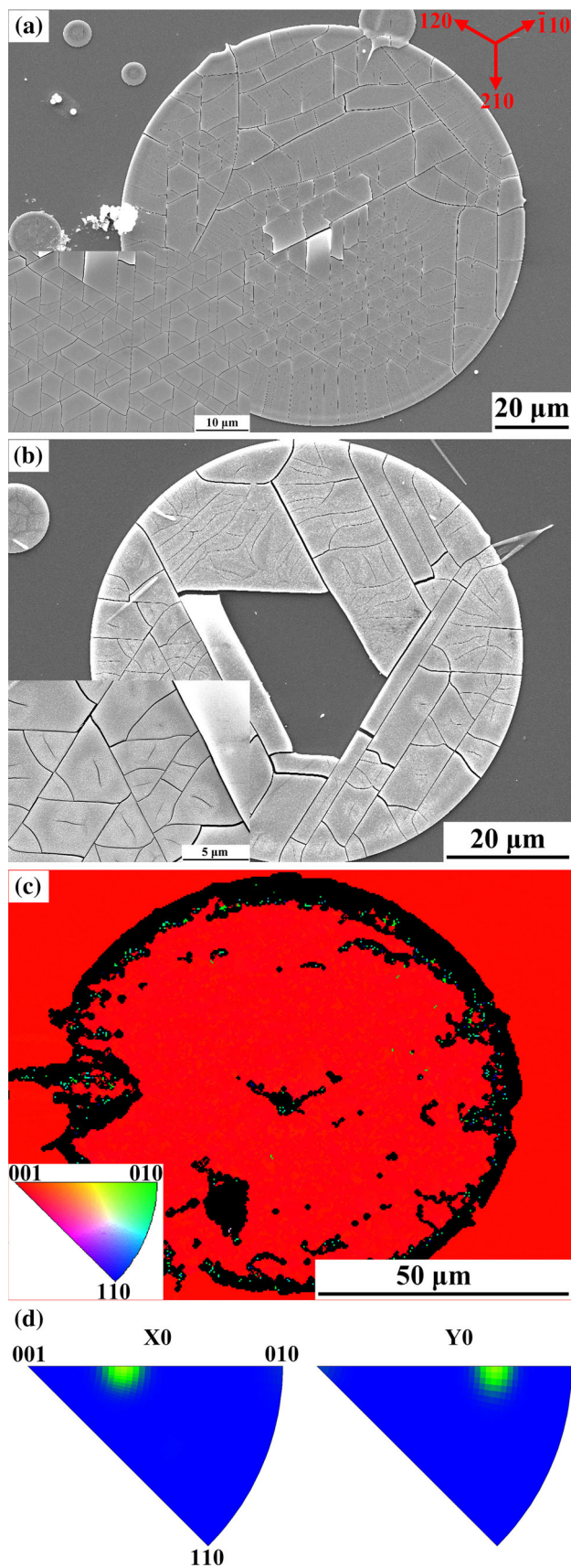


Fig. 2 Crack patterns of TiO_2 splat on Al_2O_3 substrate at the substrate temperature of (a) 100 and (b) 600 °C. Orientation maps (c) and IPFs (d) of splat deposited at 200 °C by EBSD which reveal epitaxial growth along the $\langle 012 \rangle$ (X0) and $\langle 011 \rangle$ (Y0) directions. Triangle/parallelogram crack patterns along $\langle 11 \bar{2} 0 \rangle$ direction and interface delamination are observed

spacing was quite small and substrate spallation occurred readily. These indicated that high stress was produced during splat deposition.

Bonding Condition for LCO Splats

LCO is considered as a candidate material for next generation TBCs due to its low thermal conductivity and high phase stability (Ref 30). Double-layer YSZ/LCO is also employed to combine both advantages (Ref 31). In this study, the bonding of LCO on YSZ was concerned. Epitaxial growth occurred readily at the substrate temperature merely higher than 100 °C though the lattice mismatch was as high as 9.26%. In addition, the entire splat was cut into rectangular patterns with $\langle 110 \rangle$ cracking, as shown in Fig. 4(a) and (b). Interestingly, both rough and smooth surfaces were observed. The former corresponded to La/Ce ratio close to 1:1 by energy-dispersive spectroscopy analysis (SEM–EDS), while the latter slightly lower than 1:1. Moreover, interface delamination occurred at substrate temperature below 200 °C and substrate spallation (see arrows in Fig. 4b) took place above 300 °C. The EBSD orientation maps revealed epitaxial growth along the $\langle 100 \rangle$ direction, as shown in Fig. 4(c) and Table 2. Furthermore, the crack spacing can be as small as $\sim 1 \mu\text{m}$ which was comparable to the film thickness (0.5–1 μm). This clearly suggested that enormous stress developed during splat deposition (Ref 27–29).

Bonding Condition for Cr_2O_3 Splats

Cr_2O_3 coatings are widely used as wear-resistant materials due to high hardness and toughness. In this study, epitaxial growth on Al_2O_3 , YSZ, and MgO substrates was explored. Unfortunately, dispersed particles were ubiquitous on Cr_2O_3 surfaces, which significantly increased the roughness and deteriorated the detection ability of EBSD.

The lattice mismatch between Cr_2O_3 and Al_2O_3 at room temperature was 4.07%. The splats on Al_2O_3 substrate presented quite different pattern morphologies in the central and peripheral regions, as shown in Fig. 5(a). Crack patterns in the peripheral region had irregular morphologies with many microdefects (see inset in Fig. 5a). Apparently, cracks in the peripheral region propagated by the coalescence of microdefects, forming zigzag cracking

Table 2 Corresponding crystal orientations between splats and single-crystal substrates

Splat Substrate	Lattice constant (Å)	Crystal structure	Corresponding crystal orientations			Cracking direction
			X	Y	Z	
<i>TiO₂</i>	4.594	Tetragonal	<100>	<010>	<001>	<110>, <100>
TiO ₂	4.594	Tetragonal	<100>	<010>	<001>	
<i>TiO₂</i>	4.594	Tetragonal	<011>	<012>	<001>	<11 $\bar{2}$ 0>
Al ₂ O ₃	4.758	Hexagonal	<11 $\bar{2}$ 0>	<01 $\bar{1}$ 0>	<0001>	
<i>TiO₂</i>	4.594	Tetragonal	<100>	<010>	<001>	<110>, <100>, <025>
YSZ	5.141	Cubic	<100>	<010>	<001>	
<i>LCO</i>	5.666	Cubic	<100>	<010>	<001>	<110>
YSZ	5.141	Cubic	<100>	<010>	<001>	
<i>Cr₂O₃</i>	4.960	Hexagonal	<01 $\bar{1}$ 0>	<11 $\bar{2}$ 0>	<0001>	<11 $\bar{2}$ 0>, <1 $\bar{1}$ 00>
Al ₂ O ₃	4.758	Hexagonal	<01 $\bar{1}$ 0>	<11 $\bar{2}$ 0>	<0001>	
<i>Cr₂O₃</i>	4.960	Hexagonal	<11 $\bar{2}$ 0>	<01 $\bar{1}$ 0>	<0001>	<110>
YSZ	5.141	Cubic	<100>	<010>	<001>	
γ -Al ₂ O ₃	3.950	Cubic	<101>	<112>	<111>	<110>, <120>, <100>
α -Al ₂ O ₃	4.758	Hexagonal	<11 $\bar{2}$ 0>	<01 $\bar{1}$ 0>	<0001>	

The materials with italics represented the splats

paths. However, crack patterns in the central region presented triangle/parallelogram morphologies along the <11 $\bar{2}$ 0> direction. The orientation maps indicated epitaxial growth along the <11 $\bar{2}$ 0> direction when the substrate temperature was above 500 °C, as shown in Fig. 5(b) and Table 2. In addition, the high density of cracks clearly indicated that enormous cracking stress was produced during splat deposition (Ref 27–29).

The lattice mismatch between Cr₂O₃ and YSZ at room temperature was – 3.65%. Most of the crack patterns presented regular morphologies at the substrate temperature only higher than 100 °C, as shown in Fig. 6(a). Orientation maps revealed epitaxial growth along the <100> direction, as shown in Fig. 6(b) and Table 2. In addition, the cracks were mainly along the <110> direction of YSZ substrate. Substrate cracking (arrows in Fig. 6a) was also observed at the periphery of splats due to the edge effect (Ref 22). Moreover, substrate spallation occurred readily (see inset in Fig. 6a), which was attributed to the much higher strength of Cr₂O₃ relative to that of YSZ (Ref 26). Furthermore, the crack patterns had width as large as 50 μm. All of these indicated large stress was developed during splat deposition.

Unfortunately, the epitaxial growth of Cr₂O₃ splats on MgO substrate was not detected by EBSD. The lattice mismatch between the two at room temperature was 13.79%. However, the crack patterns on MgO substrate usually presented large scales with width of 30–40 μm, as shown in Fig. 7. In addition, the cracks were approximately along the <110> direction of MgO substrate. Interestingly,

the cracks extended to the substrate and delamination was rarely observed, which was probably attributed to the much higher strength of Cr₂O₃ relative to that of MgO (Ref 26).

Bonding Condition for Al₂O₃ Splats

Al₂O₃ coatings are widely utilized as wear-resistant materials due to high hardness and good heat conduction. In this study, the bonding mechanism of Al₂O₃ on Al₂O₃ and TiO₂ was investigated. The crack patterns on Al₂O₃ substrate usually presented irregular morphologies, even though the substrate temperature was 600 °C, as shown in Fig. 8. Only weak trends of <110> or <100> cracking emerged. Large grains and intergranular cracking were clearly observed, as shown in Fig. 8(a), which revealed that few grains were formed during splat deposition. Approximately, epitaxial growth was considered to take place when the substrate temperature was above 300 °C. In the meantime, substrate spallation occurred violently, as shown in Fig. 8(b). Compared with high strength of α -Al₂O₃ (Ref 26), the spallation obviously revealed that enormous tensile stress (several GPa) was produced during splat deposition. The orientation maps of Al₂O₃ were hardly obtained by EBSD due to high residual stress or other some reasons. Fortunately, the orientation maps of the splat at 600 °C were obtained, as shown in Fig. 8(c). Interestingly, the Euler's color indicated that epitaxial growth occurred at the center forming α -Al₂O₃ (hexagonal), and in the outer region forming γ -Al₂O₃ (cubic). The corresponding orientations between γ - and α -Al₂O₃

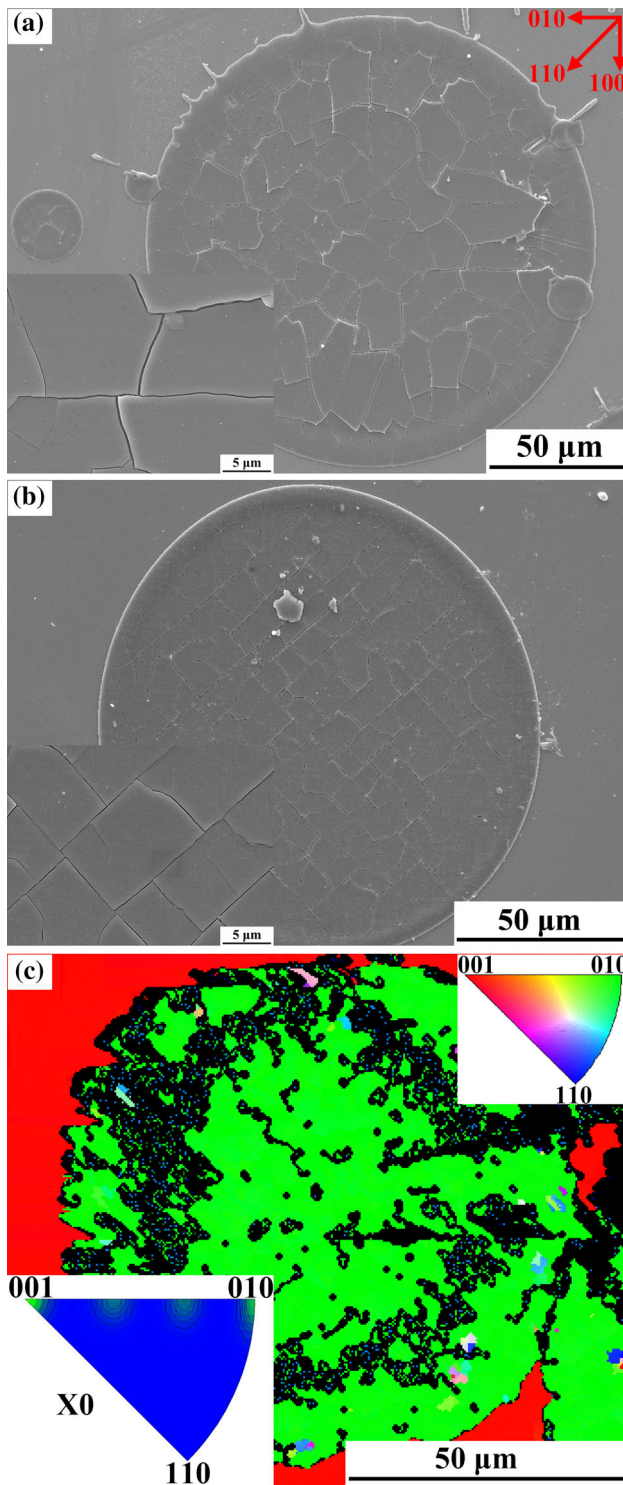


Fig. 3 Crack patterns of TiO_2 sput on YSZ substrate at the substrate temperature of (a) 300 and (b) 600 °C. (c): orientation maps of sput deposited at 300 °C by EBSD which reveal epitaxial growth mainly along the $\langle 100 \rangle$ direction. Weak trends of $\langle 100 \rangle$ and $\langle 110 \rangle$ cracking emerge

were $\langle 101 \rangle / \langle 11\bar{2}0 \rangle$ and $\langle 112 \rangle / \langle 01\bar{1}0 \rangle$, as shown in Table 2. The lattice mismatch between γ - (3.95 Å) and α -

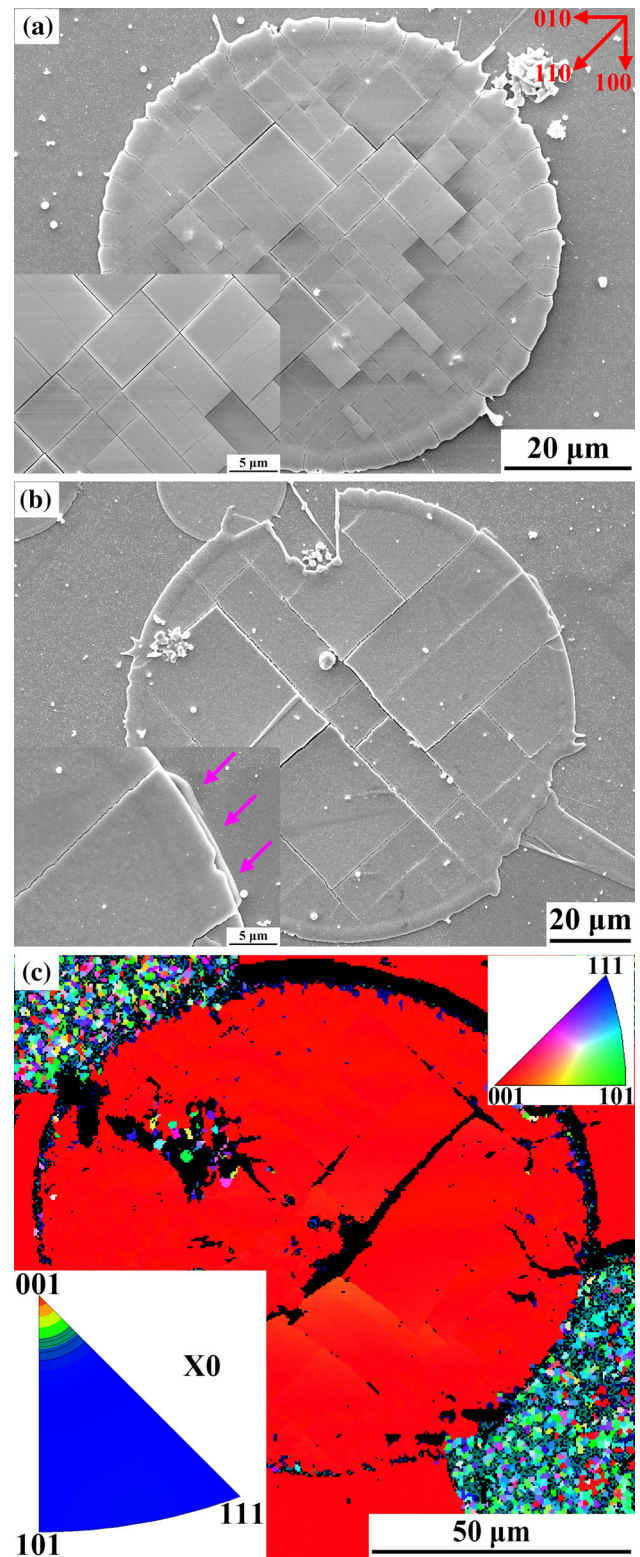


Fig. 4 Crack patterns of LCO sput on YSZ substrate at the substrate temperature of (a, b) 300 °C. (c): orientation maps of sput deposited at 200 °C by EBSD which reveal epitaxial growth along the $\langle 100 \rangle$ direction. The colorful region in (c) corresponded to the rough surface. All cracks are along $\langle 110 \rangle$ direction with exceptionally small crack spacing

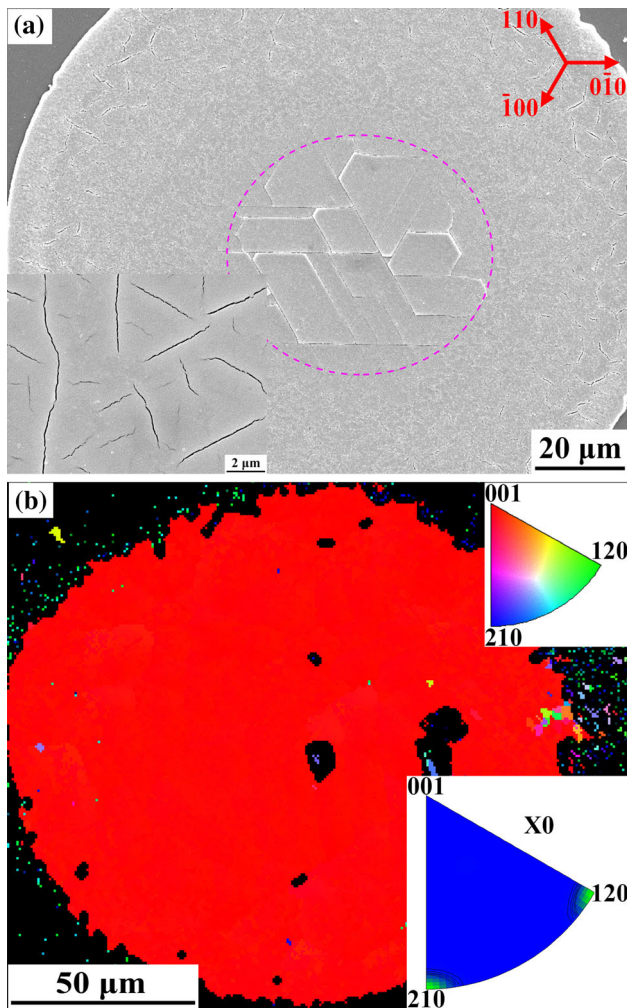


Fig. 5 Crack patterns of Cr_2O_3 splat on Al_2O_3 substrate at the substrate temperature of (a) 500 °C. (b): orientation maps of splat deposited at 500 °C by EBSD which reveal epitaxial growth along the $\langle 01\bar{1}0 \rangle$ direction. Microdefects and $\langle 11\bar{2}0 \rangle$ cracking are found in the periphery and center region, respectively

Al_2O_3 (4.758 Å) at room temperature was -20.46% . This significantly increased the quantity of microdefects leading to irregular cracking.

The crack patterns of Al_2O_3 on TiO_2 substrate were irregular with rough surfaces. In addition, the EBSD detection of Al_2O_3 splat on TiO_2 substrate failed. However, large grains and substrate spallation were clearly observed, which indicated that large tensile stress was produced during splat deposition.

Bonding Condition for LSCO Splats

LSCO is widely used as a cathode material in SOFCs and as superconducting buffer layers. In the present study, LSCO was deposited on MgO and SrTiO_3 substrates with lattice mismatches of 9 and 2%, respectively. Interestingly,

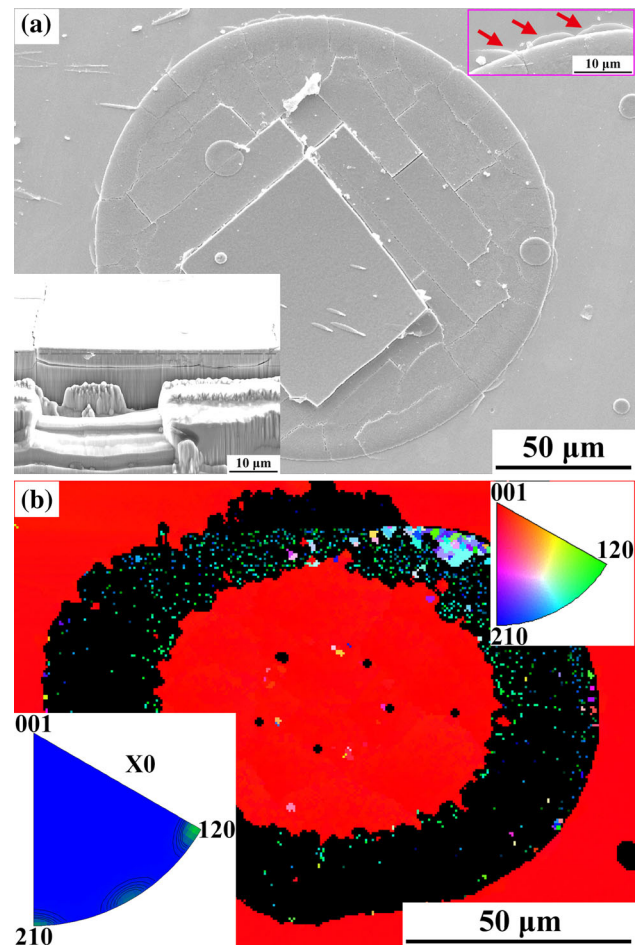


Fig. 6 Crack patterns of Cr_2O_3 splat on YSZ substrate at the substrate temperature of (a) 200 °C. The pink arrows point to substrate spallation. (b): orientation maps of splat deposited at 200 °C by EBSD which reveal epitaxial growth along the $\langle 100 \rangle$ direction (Color figure online)

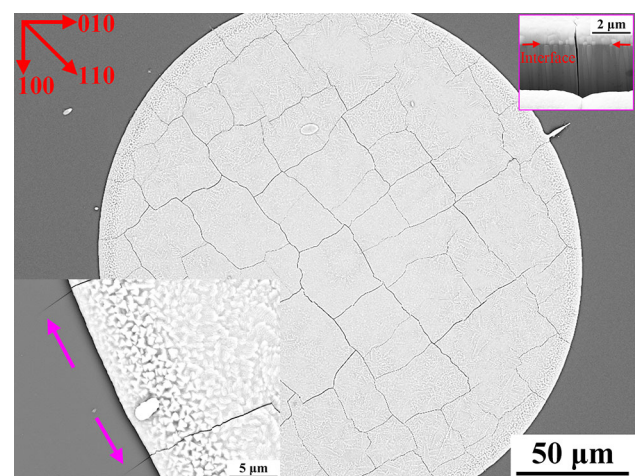


Fig. 7 Crack patterns of Cr_2O_3 splat on MgO substrate at the substrate temperature of 500 °C. The pink and red arrows point to substrate cracking and splat/substrate interface, respectively. The crack patterns are of very large size (Color figure online)

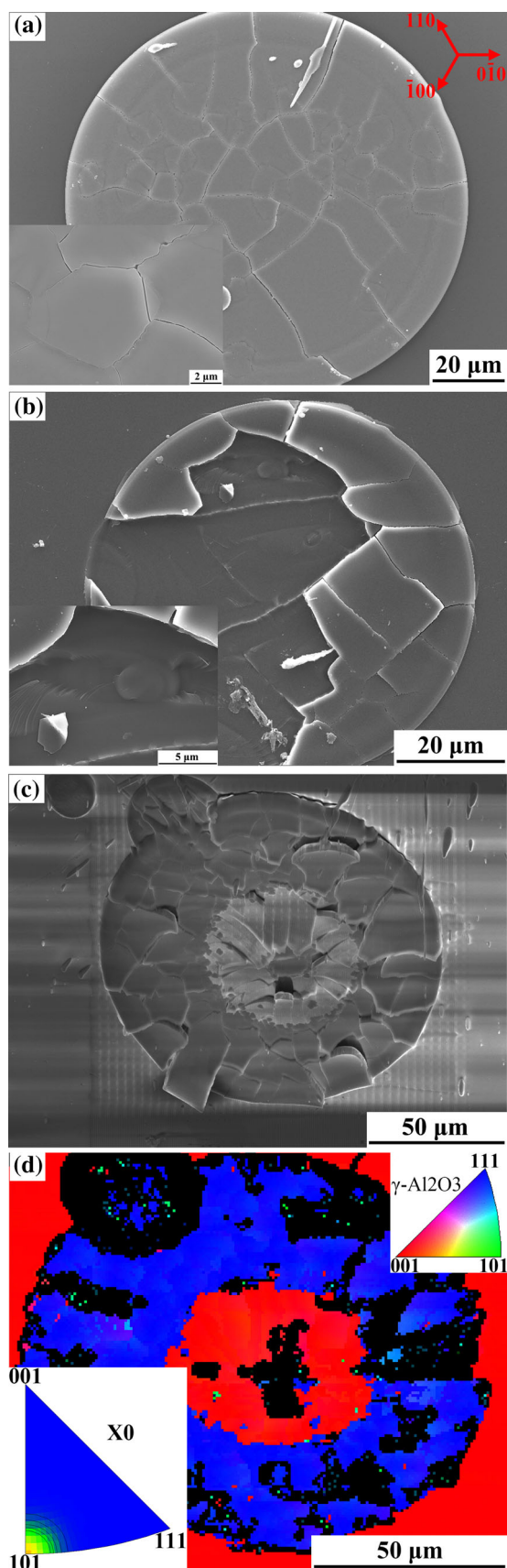


Fig. 8 Crack patterns of Al₂O₃ splat on Al₂O₃ substrate at the substrate temperature of (a) 300, (b) 500, and (c) 600 °C. Large grains and intergranular cracking (a) and substrate spallation (b) occur violently. (d): orientation maps of the splat in (c) which reveal the epitaxial growth in the central region forming α-Al₂O₃, and in the peripheral region forming γ-Al₂O₃

similar to the case on Si substrate (Ref 23), the splats presented either no cracks or perfectly hierarchical cracks on MgO substrate, as shown in Fig. 9(a). The spacing between these exquisitely carved cracks was exceptionally small, which indicated that enormous stress developed during splat deposition. In addition, interface delamination occurred on MgO substrate. However, EBSD detection on MgO substrate failed, which was attributed to the rough surface with nanoscale grains or amorphous particles.

LSCO splats on SrTiO₃ substrate presented regular morphologies, as shown in Fig. 9(b) and (c). Both interface delamination and substrate spallation took place at substrate temperature below 100 °C (Fig. 9b), while pure substrate spallation occurred above 300 °C (Fig. 9c). Interestingly, step-like hills remained on the bare substrate (see pink arrows in Fig. 9c), which were similar to steps piled up by the screw dislocations. Puzzlingly, all EBSD detections failed, which probably resulted from the rough surface consisting of nanocrystallines. Compared to the high substrate temperature (600 °C), the melting temperature of LSCO was low (1500 °C). The nanocrystallines indicated that the solidification of LSCO needed further deep exploration.

Discussion

Special Epitaxial Growth

In the present study, we report the epitaxial growth of various splat/substrate combinations at low substrate temperature (100 °C) and large lattice mismatch (− 11.26%), as shown in Table 3. To fulfill epitaxial growth, three conditions should be preferentially met: appropriate lattice mismatch, similar crystal structure, and proper substrate temperature. Generally, the allowable lattice mismatch is less than 10% for vapor phase epitaxial growth, 1% for liquid-phase epitaxial growth, and 0.1% for heterojunctions. Till now, the maximum allowable mismatch is ~ 13.9% between GaN and Al₂O₃ (vapor epitaxial growth at ultrahigh substrate temperature (900 °C) (Ref 32, 33), and ~ 13% between ZnO and Au (aqueous solution method) (Ref 34). It should be noted that both were at steady equilibrium states and extremely slow growths. However, the thermal spraying process is

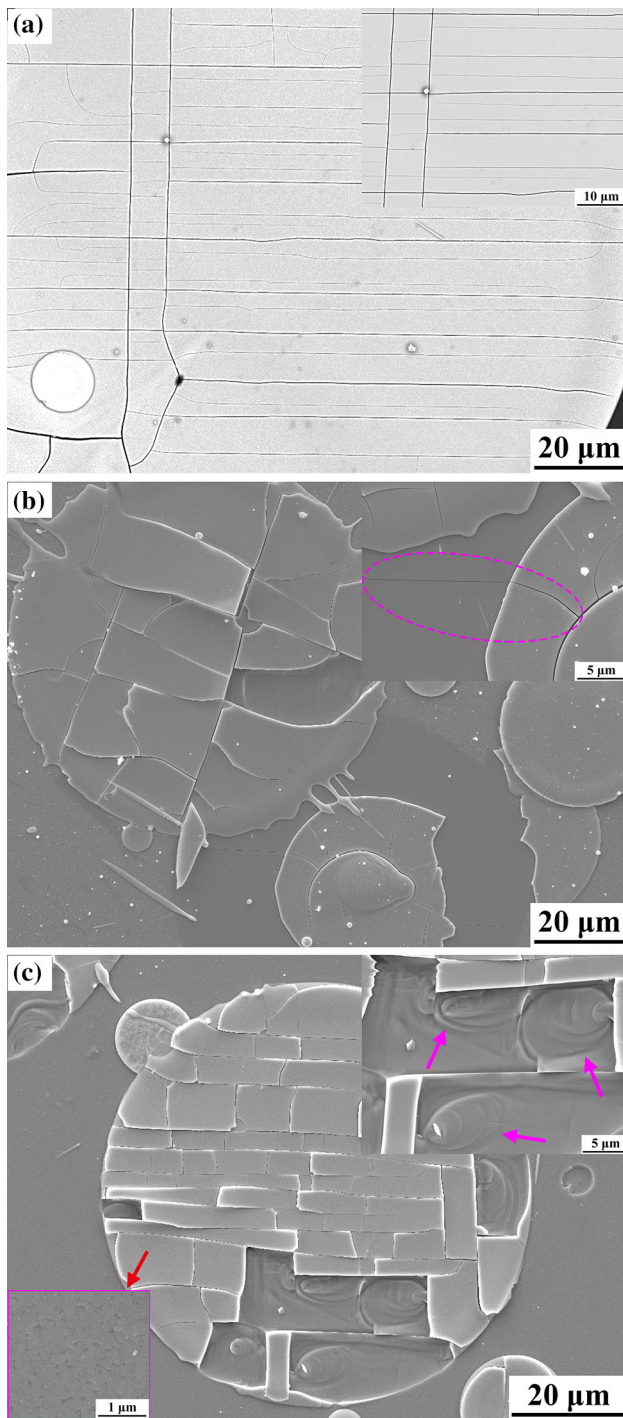


Fig. 9 Crack patterns of LSCO splat on (a) MgO and (b, c) SrTiO₃ substrate at the substrate temperature of (b) 100, (a) 500, and (c) 600 °C. The failure of EBSD detection might be due to the rough surface (red arrows in c). The pink arrows in (b) point to residual step-like hills (Color figure online)

characterized by prohibitively rapid cooling (10^4 – 10^6 K/s) (Ref 35), which severely deteriorates the capability for epitaxial growth. To our surprise, epitaxial growth did occur over a broad range of splat/substrate/temperature

combinations. There should be other factors besides rapid cooling that dominated the special large mismatch and low deposition temperature epitaxial growth.

From the epitaxial growth perspective, thermal spray deposition was essentially a liquid-phase epitaxy process (Ref 17) in which the atoms had extremely high mobility. The high-mobility atoms could rearrange readily on the exceptionally smooth substrate ($R_a \sim 0.5$ nm), in a short range and at high frequency. In addition, due to the absence of grain boundaries which probably disturbed the order of atomic arrangement, the high-mobility atoms could easily form single orientation. What is more, before epitaxial growth, the melt droplet impacted the substrate at a high speed (~ 200 m/s) (Ref 36), which enabled droplet spread at a high speed (~ 100 m/s) and in an extremely short time (~ 1 μ s) (Ref 37, 38) forming a thin liquid film. As a result, atoms in the thin liquid film only needed to diffuse and rearrange over a sufficiently short range (namely, a sufficient short time ~ 1 μ s) to fulfill large-scale uniform orientation (epitaxial growth). Compared to the characteristic time for short-range diffusion (~ 1 μ s), the characteristic time for solidification of thermal spray splats was as large as 10–20 μ s (Ref 37, 38). Therefore, both high mobility and short-range diffusion contributed to the anomalous liquid-phase epitaxy. Consequently, thermal spray deposition was easy to form chemical bonding.

Interface Temperature After Epitaxial Growth

Epitaxial growth means complete contact between splat and substrate during solidification and cooling. Apparently, the temperature of splats decreases continually from melting temperature to deposition temperature at a high cooling rate. Meanwhile, stress is considered to develop when liquid epitaxial growth completes (the liquid cannot sustain the stress). Therefore, it is important to know the interface temperature when liquid epitaxial growth is completed.

Obviously, the heat of the molten splat is mainly dissipated by three mechanisms, as shown in Fig. 10. They are thermal radiation, natural convection at the air/splat interface, and heat conduction to the substrate. Energy conservation in the molten splat and external system dictates:

$$Q_{\text{loss}} = Q_{\text{radi}} + Q_{\text{conv}} + Q_{\text{cond}} \tag{Eq 1}$$

Thermal radiation is reported to be pronounced at high temperature (~ 2000 K). The heat flux of molten splat due to thermal radiation can be expressed by Ref 39:

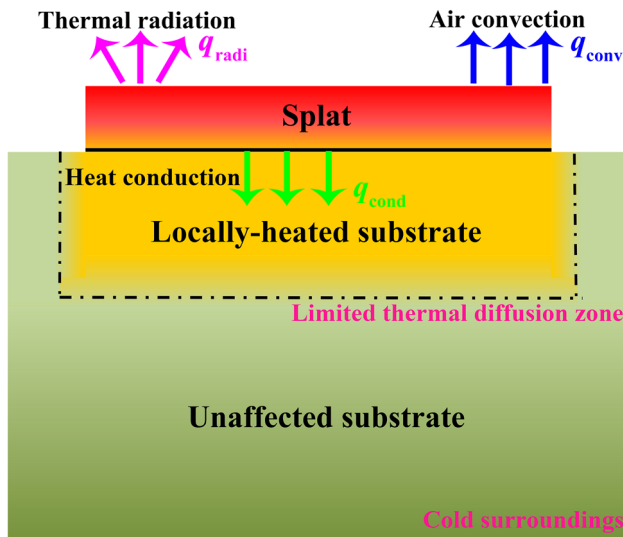
$$q_{\text{radi}} = \varepsilon\sigma T^4 \tag{Eq 2}$$

where ε and σ are emissivity (herein ~ 0.8) and Stefan-Boltzmann constant (5.67×10^{-8} W m⁻² K⁻⁴), respectively. The heat dissipation by thermal radiation follows:

Table 3 Epitaxial splat/substrate temperature combinations

Splat Substrate	TiO ₂ TiO ₂	TiO ₂ Al ₂ O ₃	TiO ₂ YSZ	LCO YSZ	LZO YSZ	YSZ YSZ	Cr ₂ O ₃ YSZ	Cr ₂ O ₃ Al ₂ O ₃	γ-Al ₂ O ₃ α-Al ₂ O ₃
<i>T_d</i> (K)	373	373	573	373	373	373	473	773	573
<i>T_i</i> (K)	1117	1052	1278	1033	1048	1386	1439	1482	1258
<i>ε_i</i> (%)	0	− 3.57	− 11.91	9.26	4.72	0	− 3.65	4.07	3.42
<i>ε_m</i> (%)	0.68	0.62	0.65	0.86	0.61	1.04	0.82	0.60	− 0.58
<i>ε_t</i> (%)	0.68	− 2.95	− 11.26	10.12	5.33	1.04	− 2.83	4.67	4.00

T_d: the lowest substrate temperature, *T_i*: the estimated interface temperature after 10 μs of heat conduction, *ε_i*: lattice mismatch at room temperature based on the corresponding crystallographic orientation, *ε_m*: mismatch strain due to the confined substrate, *ε_t*: true mismatch strain during epitaxial growth, the negative sign represented the tensile strain

**Fig. 10** The schematic diagram of the heat transfer of molten splats during solidification

$$Q_{\text{radi}} = \int_0^{t_c} q_{\text{radi}} dt \leq \varepsilon \sigma T_m^4 t_c \sim \rho C_{\text{pl}} \delta \Delta T \quad (\text{Eq 3})$$

where ρ , C_{pl} , δ , and T_m are the density, heat capacity, thickness, and melting temperature of the molten splat, respectively. Taking TiO₂ as an example, the temperature change due to thermal radiation is only about 5 °C. This indicates that thermal radiation can be negligible over such a short time ($\sim 10 \mu\text{s}$).

Heat dissipation by natural convection at the air/splat interface dictates (Ref 39):

$$Q_{\text{conv}} = \int_0^{t_c} q_{\text{conv}} dt = \int_0^{t_c} h(T - T_{\text{gas}}) \leq h T_m t_c \sim \rho C_{\text{pl}} \delta \Delta T \quad (\text{Eq 4})$$

where h is the heat transfer coefficient ($\sim 10 \text{ W m}^{-2} \text{ K}^{-1}$). Taking TiO₂ as an example, the temperature difference of the molten splat is nearly zero. This indicates that heat convection is also negligible over such a short time ($\sim 10 \mu\text{s}$).

Table 4 Parameters of thermal and mechanical property adopted in this study (Ref 41)

Parameter	TiO ₂	Al ₂ O ₃	YSZ	LCO	LZO	Cr ₂ O ₃
λ (W m ⁻¹ K ⁻¹)	3.3	5	3	0.9	1.56	5
ρ (kg m ⁻³)	4260	2900	5890	4300	4590	5210
C_{pl} (J kg ⁻¹ K ⁻¹)	1257	1888	713	470	540	1032
C_{ps} (J kg ⁻¹ K ⁻¹)	962	1272	605	430	490	891
h_c (μm)	2.8	3.7	2.9	2.1	2.5	3.0
α (10 ⁻⁶ K ⁻¹)	9.2	8.5	10.3	13	9.1	8.5
T_m (K)	2130	2323	2950	2573	2573	2603
T_g (K)	1400	1350	2000	1800

Therefore, the heat of the molten splat is mainly dissipated by heat conduction of the substrate. It was reported that the solidification time of the molten droplet was about 10–20 μs (Ref 37, 38), which indicated that the depth of thermal conduction was limited (Fig. 10). Based on dimensional analysis, the effective depth of thermal conduction in substrate follows (Ref 40):

$$h_c = \sqrt{t_c \lambda / \rho C_{\text{ps}}} \quad (\text{Eq 5})$$

which is shown in Table 4. Energy conservation of heat conduction in the substrate dictates (Ref 39):

$$\partial T / \partial t = \frac{1}{\rho C_{\text{ps}}} \frac{\partial q_{\text{cond}}}{\partial x} = D \partial^2 T / \partial x^2 \quad (\text{Eq 6})$$

where D is the thermal diffusivity equaling $\lambda / \rho C_{\text{ps}}$. This is a partial differential equation similar to the governing equation of Fick's second law. Apparently, the solution depends on the boundary conditions. However, this is a complex transient-state process with prohibitively short time and continually changing boundary temperature. Till now, an analytical solution has not been obtained.

Approximately, the temperature in molten splat is assumed to be uniform because natural convection and heat conduction can easily take place in the interior of such thin liquid film ($\sim 1 \mu\text{m}$ thick). More importantly, the

treatment similar to the drive in diffusion (Ref 24) is adopted, namely, the temperature in heat conduction zone following normal distribution, which dictates:

$$T(x, t) - T_d = \frac{A_0}{\sqrt{\pi Dt/8}} e^{-2x^2/Dt} \tag{Eq 7}$$

where A_0 derives from energy conservation (Eq 1). It can be expressed by:

$$A_0 = \frac{\rho_l C_{pl}}{\rho_s C_{ps}} \delta (T_m - T_i) \tag{Eq 8}$$

then the interface temperature becomes:

$$T(0, t) = \frac{\frac{\rho_l C_{pl}}{\rho_s C_{ps}} \delta T_m + \sqrt{\pi Dt/8} T_d}{\frac{\rho_l C_{pl}}{\rho_s C_{ps}} \delta + \sqrt{\pi Dt/8}} \tag{Eq 9}$$

When adopting the property parameters in Table 4, the interface temperature is shown in Fig. 11. In addition, the interface temperature after 10 μ s of heat conduction (shown in Table 3) is lower than the glass transition temperature (T_g , shown in Table 4) reported by Chase (Ref 41) which is the lowest limit temperature for epitaxial growth.

The low interface temperature clearly suggests that epitaxial growth or solidification has ended before 10 μ s of heat conduction with high cooling rates ($\sim 10^8$ K s⁻¹). In conventional vapor epitaxial growth, to promote atom diffusion and rearrangement (Ref 25), the substrate temperature is made high, leading to long epitaxial growth times (several hours or days). The extremely short growth time (< 10 μ s) here clearly reveals that thermally sprayed deposition is an anomalous liquid-phase epitaxial growth. Apparently, long-range diffusion of atoms is not available over such a short time. This further demonstrates that atoms only need to diffuse and rearrange over a sufficiently short range for large-scale epitaxial growth during splat deposition.

Cracking of Chemical Bonding Region

Epitaxial growth indicated the formation of chemical bonding and complete contact between the splat and the substrate. However, transverse gaps either at the interface or in the substrate were ubiquitous besides vertical cracks. There also existed pure transverse gaps in YSZ, LSCO, and TiO₂ splats, but no vertical cracks. These revealed that enormous tensile stresses were produced during splat deposition. Apparently, the stress was related to the deposition process. Generally, thermal spray deposition experienced three stages, namely, droplet impacting and spreading, liquid splat solidifying, and solid splat cooling. The fact that liquid film cannot sustain the stress should be remembered and obeyed. Therefore, cracks are produced during splat cooling. As stated before, heat conduction in

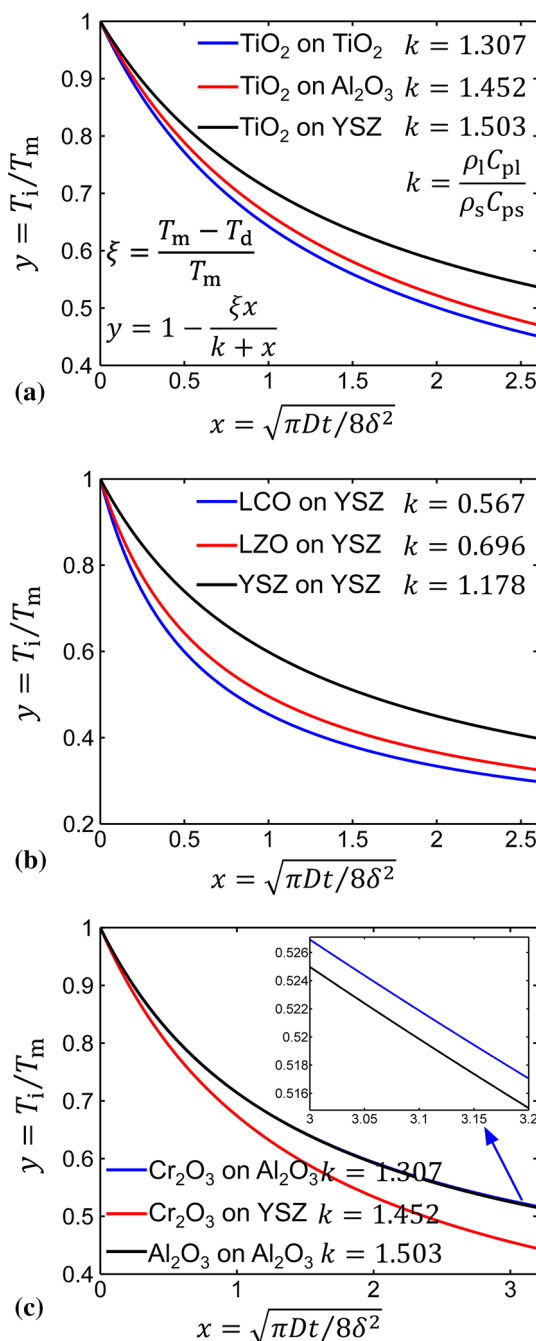


Fig. 11 Normalized interface temperature related to normalized solidification time. (a): tetragonal TiO₂ splats on TiO₂, Al₂O₃, and YSZ substrate. (b): cubic LCO, LZO, and YSZ splats on YSZ substrate. (c): hexagonal Cr₂O₃ splats on Al₂O₃ and YSZ substrate as well as Al₂O₃ splats on Al₂O₃ substrate

the substrate is the only effective way of heat transfer. The depth of heat conduction enlarges continually during splat cooling (Fig. 10). Meantime, the temperature of the solid splat decreases.

In general, quenching stress was regarded as the reason for cracking. However, the heat conduction zone was always constrained by its cold surroundings (Fig. 10). This

indicated that the heat conduction zone did not involve shrinkage. Consequently, the quenching stress was mainly from the temperature difference in the splat. In conjunction with Eq 7, the maximum temperature difference related to the splat thickness follows:

$$T_i - T \approx (T_i - T_d) \cdot \left(1 - e^{-2\delta^2/Dt}\right) \quad (\text{Eq 10})$$

For the TiO₂ splat, the maximum temperature difference is about 164 K, corresponding to strain of ~ 0.15%. The temperature difference in the splat was small due to its being extremely thin. Therefore, there should be other stress producing mechanisms.

In fact, the splat was much smaller than the substrate, and only the localized substrate was strongly heated by molten splat, as shown in Fig. 10 (the yellow region). However, this localized substrate was strictly constrained by its cold surroundings. This indicated that the lattice parameter of the localized substrate was always identical to this at the initial substrate temperature. Therefore, lattice mismatch between the splat and the localized substrate was produced. The lattice mismatch was relieved by dislocations during solidification (the liquid film cannot sustain the stress), and by stress driven cracking during cooling. The mismatch strain dictates:

$$\varepsilon_m = \alpha \cdot (T_i - T_d) \quad (\text{Eq 11})$$

where α is the thermal expansion coefficient, and T_i the interface temperature when epitaxial growth is completed; here, it is assumed to be the value after 10 μ s of heat conduction. As a result, constraint of the locally heated substrate by its cold surroundings produces a large mismatch strain, as shown in Table 3.

Besides interfacial delamination of LZO splats on YSZ substrate below 300 °C (Ref 17, 22), YSZ and LCO splats on YSZ substrate below 100 °C, and TiO₂ splats on Al₂O₃ substrate below 600 °C (Fig. 2b), substrate spallation occurred in all other kinds of splat/substrate combinations. This seems inconsistent with the fact that inter-lamellar transverse delamination mainly occurred in real coatings. Due to high cooling rates and the constraint of the locally heated substrate (Fig. 10), large numbers of defects such as dislocations and stacking faults were formed at epitaxial splat/substrate interface (Ref 42). This results in the lamellar interface having lower cracking resistance and being vulnerable to delamination. In addition, thermal spray coatings are layered materials. For a splat deposited on layered substrate, transverse pores can be formed by delamination at both splat/substrate interface and inter-lamellar interface in layered substrate. Therefore, the transverse pores in thermal spray coatings are mainly from substrate spallation at inter-lamellar interface of the layered substrate. This is consistent with the fact that the spacing of

lamellar pores in the thickness direction (namely the thickness of intact lamellae) is generally several times splat thickness.

Cracking Path Selection

Interestingly, different splat/substrate combinations presented diverse crack patterns such as rectangular along $\langle 110 \rangle$ and parallelograms along $\langle 11\bar{2}0 \rangle$ in the TiO₂/TiO₂ and TiO₂/Al₂O₃ systems, as shown in Fig. 1 and 2, respectively. What does determine the shapes of the crack patterns? It was reported that the cracking followed the path with either greatest motivation or least resistance (Ref 42-46). When various cracking modes existed, the cracking path favored where the largest ratio of cracking motivation to resistance was located (Ref 43-47).

Generally, the cleavage planes/directions are parallel to the closest-packed planes/directions because lattice distortion in the closest-packed planes/directions is the severest. This produces intrinsic preferential cracking orientations of least resistance. As expected, when cubic LC/LZ/YSZ on YSZ, the cracks are always along the $\langle 110 \rangle$ direction. Similarly, the cracking of tetragonal TiO₂ on TiO₂ is orientated along the $\langle 110 \rangle$ direction (a few along $\langle 100 \rangle$), consistent with the cleavage direction of TiO₂. For hexagonal Cr₂O₃ on Al₂O₃, parallelogram or triangle crack patterns are formed along the $\langle 11\bar{2}0 \rangle$ or $\langle 1\bar{1}00 \rangle$ direction with 120° angles.

However, the crack patterns become a bit complex for splats on heterostructured substrates. Considering TiO₂ on Al₂O₃, the cracks are oriented along $\langle 120 \rangle$ and a few along $\langle 100 \rangle$, forming triangles or parallelograms with 60° angles. The $\langle 11\bar{2}0 \rangle$ direction is the basal orientation and also the closest-packed direction of hexagonal Al₂O₃. Therefore, the crystal structures of both the splat and substrate dominate crack patterns. The cracking of hexagonal Cr₂O₃ on cubic YSZ is another case. Since the strength of YSZ is much lower than that of Cr₂O₃ (Ref 26), the cracks preferentially orientated along the $\langle 110 \rangle$ direction of YSZ splat, despite of the cleavage of Cr₂O₃.

When tetragonal TiO₂ splat was deposited on cubic YSZ substrate, epitaxial growth is incomplete due to the extremely large lattice mismatch (~ - 11.26%). However, all the grains are orientated along $\langle 001 \rangle$ in the z direction and only along $\langle 011 \rangle$, $\langle 010 \rangle$, and $\langle 012 \rangle$ in x/y directions. Due to ubiquitous microdefects, cracks propagate through the coalescence of these microdefects. Therefore, the cracks seem quite irregular and locally orientated along the $\langle 110 \rangle$ or $\langle 100 \rangle$ direction. Epitaxial growth of cubic γ -Al₂O₃ on hexagonal α -Al₂O₃ is exceptionally difficult because the lattice mismatch between γ -Al₂O₃ (3.95 Å) and α -Al₂O₃ (4.758 Å) is as high as - 20.46%, with

different crystal structures. One way to alleviate the mismatch is the rotation of the lattice. As a result, the corresponding orientations between epitaxial γ -Al₂O₃ and α -Al₂O₃ are $\langle 121 \rangle / \langle 01\bar{1}0 \rangle$ and $\langle 110 \rangle / \langle 11\bar{2}0 \rangle$. The lattice mismatch of the former is about 3.42% and the latter 14.82%. This indicates the quality of epitaxy is quite imperfect and substantial microdefects exist. As expected, the cracks seem irregular and only weak trends emerge along the $\langle 110 \rangle$, $\langle 100 \rangle$, and $\langle 120 \rangle$ directions.

In short, both of the crystal structures of the splat and substrate and the distribution of microdefects determine cracking paths. It should be noted that all cracking paths in the present study rely on the least resistance. This again indicates that the tensile stresses are large enough and not the limiting conditions for driving cracking.

Abnormal Case of Al₂O₃ on TiO₂ and LSCO on SrTiO₃

Compared to TiO₂ on Al₂O₃, the epitaxial growth of Al₂O₃ on TiO₂ failed and the cracks seemed quite irregular. Considering the case of Al₂O₃ on Al₂O₃, EBSD orientation maps revealed that the splat was cubic (γ -phase) when the substrate temperature was below 500 °C. The lattice mismatch between cubic γ -Al₂O₃ (3.95 Å) and TiO₂ (4.594 Å) was as high as – 16.3%. Due to similar crystal structures and symmetries, alleviation of the mismatch by lattice rotation seemed difficult. Up to now, there are no reports on epitaxial growth with such a large lattice mismatch by other techniques such as vapor phase epitaxy.

However, the lattice mismatch between LSCO and SrTiO₃ at room temperature was only – 2%. It was puzzling that epitaxial growth of LSCO on SrTiO₃ failed even when the substrate temperature reached 600 °C. The surface microstructure indicated that polycrystalline LSCO was formed at all substrate temperatures. The reason remained unclear and need further exploration.

Conclusion

In the present study, we report the epitaxial growth of various splat/substrate combinations by thermal spray technology at very low substrate temperature (100 °C) and large lattice mismatch (– 11.26%). To fulfill epitaxial growth, three conditions should be met, namely, appropriate lattice mismatch, similar crystal structure, and proper substrate temperature. Essentially, thermally sprayed deposition is a liquid-phase epitaxy process and easy to form chemical bonding. The interface temperature was estimated and found to be quite low during solidification. This convincingly demonstrated that atoms only needed to

diffuse and rearrange over a sufficiently short range for the special liquid-phase epitaxial growth by thermally sprayed technology.

In addition, lamellar gaps were ubiquitous in the epitaxial splat/substrate system. This strongly suggested that lamellar gaps in thermally sprayed coatings mainly resulted from transverse cracking. Besides, the high-density cracks revealed that enormous tensile stresses were produced during splat deposition. Mechanical analysis showed that enormous tensile stresses resulted from constraint of the locally heated substrate by its cold surroundings. This was the essential difference between the conventional and present epitaxial technologies.

Acknowledgments The present project is supported by National Basic Research Program (Nos. 2013CB035701), the Fundamental Research Funds for the Central Universities, and the National Program for Support of Top-notch Young Professionals.

References

1. N.P. Padture, M. Gell, and E.H. Jordan, Materials Science—Thermal Barrier Coatings for Gas-Turbine Engine Applications, *Science*, 2002, **296**(5566), p 280-284
2. N.P. Padture, Advanced Structural Ceramics in Aerospace Propulsion, *Nat. Mater.*, 2016, **15**(8), p 804-809
3. R. Hui, J.O. Berghaus, C. Deces-Petit, W. Qu, S. Yick, J.G. Legoux, and C. Moreau, High Performance Metal-supported Solid Oxide Fuel Cells Fabricated by Thermal Spray, *J. Power Sources*, 2009, **191**(2), p 371-376
4. R. Vassen, D. Hathiramani, J. Mertens, V.A.C. Haanappel, and I.C. Vinke, Manufacturing of High Performance Solid Oxide Fuel Cells (SOFCs) with Atmospheric Plasma Spraying (APS), *Surf. Coat Technol.*, 2007, **202**(3), p 499-508
5. G. Bolelli, V. Cannillo, L. Lusvardi, and T. Manfredini, Wear behaviour of thermally sprayed ceramic oxide coatings, *Wear*, 2006, **261**(11–12), p 1298-1315
6. S. Wilson, Thermally Sprayed Abradable Coating Technology for Sealing in Gas Turbines, in 6th International Conference on the Future of Gas Turbine Technology, 2012
7. E. Irissou, A. Dadouche, and R.S. Lima, Tribological Characterization of Plasma-Sprayed CoNiCrAlY-BN Abradable Coatings, *J Therm. Spray Technol.*, 2014, **23**(1–2), p 252-261
8. D. Sporer, M. Dorfman, L. Xie, A. Refke, I. Giovannetti, and M. Giannozzi, Processing and Properties of Advanced Ceramic Abradable Coatings, *Therm. Spray 2007 Global Coat. Solut.*, 2007, **2007**, p 14-16
9. A. Ohmori and C.J. Li, Quantitative Characterization of the Structure of Plasma-Sprayed Al₂O₃ Coating by Using Copper Electroplating, *Thin Solid Films*, 1991, **201**(2), p 241-252
10. S. Rangarajan and A.H. King, Non-destructive Evaluation of Delamination in Ceramic Thin Films on Metal Substrates by Scanning Electron Microscopy, *Thin Solid Films*, 2001, **385**(1–2), p 22-28
11. T. Chraska and A.H. King, Effect of Different Substrate Conditions upon Interface with Plasma Sprayed Zirconia—A TEM Study, *Surf. Coat Technol.*, 2002, **157**(2–3), p 238-246
12. T. Chraska and A.H. King, Transmission Electron Microscopy Study of Rapid Solidification of Plasma Sprayed Zirconia—Part I. First Splat Solidification, *Thin Solid Films*, 2001, **397**(1–2), p 30-39

13. T. Chraska and A.H. King, Transmission Electron Microscopy Study of Rapid Solidification of Plasma Sprayed Zirconia—Part II. Interfaces and Subsequent Splat Solidification, *Thin Solid Films*, 2001, **397**(1–2), p 40–48
14. A.G. Evans, M. Ruhle, B.J. Dalgleish, and P.G. Charalambides, The Fracture Energy of Bimaterial Interfaces, *Metall. Trans. A*, 1990, **21**(9), p 2419–2429
15. C.J. Li and A. Ohmori, Relationships Between the Microstructure and Properties of Thermally Sprayed Deposits, *J Therm. Spray Technol.*, 2002, **11**(3), p 365–374
16. C.J. Li, G.J. Yang, and C.X. Li, Development of Particle Interface Bonding in Thermal Spray Coatings: A Review, *J. Therm. Spray Technol.*, 2013, **22**(2–3), p 192–206
17. L. Chen, G.J. Yang, and C.X. Li, Formation of Lamellar Pores for Splats via Interfacial or Sub-interfacial Delamination at Chemically Bonded Region, *J. Therm. Spray Technol.*, 2017, **26**, p 315–326
18. V.V. Sobolev, J.M. Guilemany, J. Nutting, and J.R. Miquel, Development of Substrate-coating Adhesion in Thermal Spraying, *Int. Mater. Rev.*, 1997, **42**(3), p 117–136
19. C.J. Li and J.L. Li, Transient Contact Pressure During Flattening of Thermal Spray Droplet and its Effect on Splat Formation, *J. Therm. Spray Technol.*, 2004, **13**(2), p 229–238
20. X.Y. Jiang, Y.P. Wan, H. Herman, and S. Sampath, Role of Condensates and Adsorbates on Substrate Surface on Fragmentation of Impinging Molten Droplets During Thermal Spray, *Thin Solid Films*, 2001, **385**(1–2), p 132–141
21. M.X. Xue, S. Chandra, and J. Mostaghimi, Investigation of Splat Curling up in Thermal Spray Coatings, *J. Therm. Spray Technol.*, 2006, **15**(4), p 531–536
22. L. Chen, G.-J. Yang, C.-X. Li, and C.-J. Li, Edge Effect on Crack Patterns in Thermally Sprayed Ceramic Splats, *J. Therm. Spray Technol.*, 2017, **26**, p 302–314
23. L. Chen, G.J. Yang, C.X. Li, and C.J. Li, Hierarchical Formation of Intrasplat Cracks in Thermal Spray Ceramic Coatings, *J. Therm. Spray Technol.*, 2016, **25**(5), p 959–970
24. S.A. Campbell, The Science and Engineering of Microelectronic Fabrication, 2nd edn, Chapter 3. *Oxford University Press*, Oxford, 2001
25. L.B. Freund and S. Suresh, *Thin Film Materials: Stress, Defect Formation, and Surface Evolution*, Cambridge University Press, Cambridge, 2003
26. J. Robertson and M.I. Manning, Limits to Adherence of Oxide Scales, *Mater. Sci. Technol.*, 1990, **6**(1), p 81–92
27. V.B. Shenoy, A.F. Schwartzman, and L.B. Freund, Crack Patterns in Brittle Thin Films, *Int. J. Fract.*, 2001, **109**(1), p 29–45
28. M.D. Thouless, Crack Spacing in Brittle Films on Elastic Substrates, *J. Am. Ceram. Soc.*, 1990, **73**(7), p 2144–2146
29. M.D. Thouless, E. Olsson, and A. Gupta, Cracking of Brittle Films on Elastic Substrates, *Acta Metall. Mater.*, 1992, **40**(6), p 1287–1292
30. X. Cao, R. Vassen, W. Fischer, F. Tietz, W. Jungen, and D. Stöver, Lanthanum-Cerium Oxide as a Thermal Barrier-Coating Material for High-temperature Applications, *Adv. Mater.*, 2003, **15**(17), p 1438–1442
31. W. Ma, S. Gong, H. Li, and H. Xu, Novel Thermal Barrier Coatings Based on La₂Ce₂O₇/8YSZ Double-Ceramic-Layer Systems Deposited by Electron Beam Physical Vapor Deposition, *Surf. Coat Technol.*, 2008, **202**(12), p 2704–2708
32. S. Kaiser, H. Preis, W. Gebhardt, O. Ambacher, H. Angerer, M. Stutzmann, A. Rosenauer, and D. Gerthsen, Quantitative Transmission Electron Microscopy Investigation of the Relaxation by Misfit Dislocations Confined at the Interface of GaN/Al₂O₃ (0001), *Jpn. J. Appl. Phys.*, 1998, **37**(1), p 84–89
33. A.F. Schwartzman and R. Sinclair, Metastable and Equilibrium Defect Structure of II–VI/GaAs Interfaces, *J. Electron. Mater.*, 1991, **20**(7), p 805–814
34. J.H. Joo, K.J. Greenberg, M. Baram, D.R. Clarke, and E.L. Hu, Aqueous Epitaxial Growth of ZnO on Single Crystalline Au Microplates, *Cryst. Growth Des.*, 2013, **13**(3), p 986–991
35. M. Vardelle, A. Vardelle, A.C. Leger, P. Fauchais, and D. Gobin, Influence of Particle Parameters at Impact on Splat Formation and Solidification in Plasma Spraying Processes, *J. Therm. Spray Technol.*, 1995, **4**(1), p 50–58
36. H. Jones, Cooling, Freezing and Substrate Impact of Droplets Formed by Rotary Atomization, *J. Phys. D Appl. Phys.*, 1971, **4**(11), p 1657–1660
37. R. McPherson, A Review of Microstructure and Properties of Plasma Sprayed Ceramic Coatings, *Surf. Coat Technol.*, 1989, **39**(1–3), p 173–181
38. C. Moreau, P. Cielo, M. Lamontagne, S. Dallaire, J.C. Krapez, and M. Vardelle, Temperature Evolution of Plasma-Sprayed Niobium Particles Impacting on a Substrate, *Surf. Coat Technol.*, 1991, **46**(2), p 173–187
39. T.L. Bergman, A.S. Lavine, F.P. Incropera, and D.P. Dewitt, *Fundamentals of Heat and Mass Transfer*, 7th ed., Wiley, New York, 2012
40. Q.M. Tan, *Dimensional Analysis. With Case Studies in Mechanics*, Springer, Berlin, Heidelberg, 2011
41. M.W. Chase, NIST-JANAF thermochemical tables. *J. Phys. Chem. Reference Data*, 1998, **9**
42. L. Chen and G.-J. Yang, Anomalous Epitaxial Growth in Thermally Sprayed YSZ and LZ Splats, *J Therm Spray Technol*, 2017, **26**(5566), p 1168–1182
43. J.W. Hutchinson and Z. Suo, Mixed-Mode Cracking in Layered Materials, *Adv. Appl. Mech.*, 1992, **29**, p 63–191
44. J.W. Hutchinson, Stresses and Failure Modes in Thin Films and Multilayers, in *Lecture Notes*, 1996
45. A. Bagchi and A.G. Evans, The Mechanics and Physics of Thin Film Decohesion and its Measurement, *Interface Sci.*, 1996, **3**(3), p 169–193
46. A.G. Evans and J.W. Hutchinson, The Thermomechanical Integrity of Thin Films and Multilayers, *Acta Metall. Mater.*, 1995, **43**(7), p 2507–2530
47. Z. Suo and J.W. Hutchinson, Steady-State Cracking in Brittle Substrates Beneath Adherent Films, *Int. J. Solids Struct.*, 1989, **25**(11), p 1337–1353